PAPER

Check for updates

Controlling interface properties for enhanced photocatalytic performance: a case-study of CuO/TiO2 nanobelts†

Huaqiang Zhuang, [ID] [ab] Siying Zhang,[a] Manru Lin,[a] Liqin Lin,[a] Zhenping Cai*[c] and Wentao Xu*[a]

TiO2 nanobelts with CuO modification were designed and fabricated *via* a facile strategy. The photocatalytic degradation of methyl orange (MO) is selected as a model reaction to investigate the photocatalytic performance of all as-prepared CuO/TiO2 nanobelts under full-spectrum light (300–2500 nm) irradiation. The optimized mass fraction of CuO is 0.1% for CuO/TiO2 composite nanobelts, namely CT-0.1 sample, which can almost completely degrade MO pollutant in 50 min. The as-obtained CuO/TiO2 composites are systematically investigated by a variety of physical and chemical characterizations. Therein, it can be obtained that superoxide radicals ($\bullet O_2^-$) and hydroxyl radicals ($\bullet OH$) are the main active species in this photocatalytic system. The photoelectrochemical measurement clearly demonstrates that the enhanced photocatalytic activity can be attributed to the efficient separation and transfer of photo-generated electron–hole pairs, and lower overpotential for CuO/TiO2 nanobelts. This work provides a prototype to study the photocatalytic oxidation process, which contributes to the design and construction of highly-efficient composite photocatalysts.

1 Introduction

Semiconductor-based photocatalysis has been verified to be an effective approach to resolve environmental and energy issues.[1–3] Among many photocatalysts, TiO2 has been considered to be one of the most promising candidates, owing to its excellent catalytic activity, stability, nontoxicity and low cost.[4–6] Nevertheless, the wide band gap and low separation and transfer efficiency of photo-generated charge carriers still limit the solar conversion efficiency and large-scale application of TiO2.[7–10] As we all know, the photocatalytic process mainly involves the following three steps.[11,12] The initial step is the generation of photo-excited hole–electron pairs in the photocatalyst under solar light irradiation. Subsequently, the photo-generated electron–hole pairs will be separated and migrate on the surface of the semiconductor photocatalyst. Finally, electrons and holes on the surface will participate in reduction and oxidation reactions to accomplish the solar energy conversion process. Thereinto, the separation of photo-generated electron–hole pairs is one of the important steps

for achieving good photocatalytic performance.[13–16] Therefore, a large number of efforts have been devoted to enhancing the separation efficiency of photo-generated electron–hole pairs to improve the photocatalytic activity.

A variety of strategies, such as metal or nonmetal doping, semiconductor compositing and cocatalyst modifying, have been developed to improve the separation and transfer efficiency of photo-generated charge carriers.[17–20] Jing *et al.*[21] reported that BiOCl was modified by RGO and phosphate groups to improve the photogenerated charge separation and photochemical stability. Similarly, some noble metals are normally regarded as active sites to enhance the separation and transfer efficiency of photo-generated electron–hole pairs. The ultrafast charge separation and long-lived charge separated state of CdS nanorods were directly demonstrated by the introduction of Pt nanoparticles.[22] In addition, some transition metal oxides, such as CuO, NiO and Co3O4, can also act as cocatalysts to improve photocatalytic performance. For example, Reddy *et al.*[23] reported that CuO quantum dots as cocatalysts could boost the photocatalytic hydrogen production of TiO2. The CuO nanoparticles were introduced on flower-like ZnO to construct a 0D–3D CuO/ZnO heterojunction, which enhanced the separation efficiency of the photogenerated electron–hole pairs resulting in enhanced photocatalytic performance.[24] Some previous reports[25–28] also demonstrate that NiO and Co3O4 can act as cocatalysts to improve the photocatalytic activity. These research studies suggest that transition

[a] *College of Chemical Engineering and Materials Science, Quanzhou Normal University, Quanzhou 362000, P. R. China. E-mail: xuwentao93@aliyun.com*

[b] *Key Laboratory of Green Energy and Environment Catalysis, Ningde Normal University, Fujian Province, Ningde, 352100, P. R. China*

[c] *Department of Chemical Engineering, Norwegian University of Science and Technology, N-7491, Trondheim, Norway. E-mail: zhenping.cai@ntnu.no*

† Electronic supplementary information (ESI) available. See DOI: 10.1039/d0ma00172d

metal oxides have considerable potential to replace noble metals and can be applied in the photocatalytic field.

CuO is a promising candidate to act as a cocatalyst, attributed to its low cost, narrow band gap and nontoxicity.[29–31] Furthermore, CuO has the ability to enhance the utilization efficiency of solar energy and accelerate the separation of photo-excited charge carriers after surface modification on TiO_2. Wang *et al.*[32] reported that CuO quantum dots incorporated into TiO_2 nanosheets could obviously improve photocatalytic water splitting performance. Lu *et al.* directly[33] revealed the role of CuO in the plasmonic photo-catalysis of $Ag/AgCl/TiO_2$, which could enhance the photocatalytic activity for degradation of methyl orange and phenol. It can be seen that the electronic band structure of CuO is very well matched with that of TiO_2, which is beneficial for the separation and transfer of photo-generated electron–hole pairs. Although lots of studies focus on the CuO/TiO_2 photocatalyst, the enhanced nature of CuO nanoparticles incorporated on TiO_2 nanobelts is still lacking in systematic research.

In this work, we show a facile method to prepare CuO/TiO_2 nanobelts for the degradation of methyl orange (MO). The composition and structure of CuO/TiO_2 nanobelts with different CuO content were systematically characterized by XRD, SEM and DRS measurements. The CT-0.1 sample displays the best photocatalytic performance compared to the others for the degradation of methyl orange (MO). Furthermore, the active species trapping experiments demonstrate that superoxide radicals ($\bullet O_2^-$) and hydroxyl radicals ($\bullet OH$) are the main active species in this photocatalytic system. The enhanced photocatalytic activity can be attributed to the efficient separation and transfer of photo-generated electron–hole pairs. In addition, the as-prepared CT-0.1 sample shows a lower overpotential, which is beneficial for photo-catalytic oxidation processes.

2 Experimental

2.1 Catalyst preparation

TiO_2 nanobelts. The TiO_2 nanobelts were synthesized *via* a typical hydrothermal method. In a typical preparation process, 0.4 g of TiO_2 power (P25) was added to 72 mL of 10 M NaOH aqueous solution under continuous ultrasound treatment for 40 min. Then, the mixed solution was transferred to a 100 mL Teflon-lined stainless steel autoclave and heated at 200 °C for 24 h. After the completion of the reaction, the as-prepared samples were washed with deionized water several times. Subsequently, the as-obtained samples were immersed in 0.1 mol L^{-1} HCl aqueous solution for 13 hours. After that, the wet products were washed until the solution pH value reached 7, and then the $H_2Ti_3O_7$ nanobelts were dried at 60 °C for 24 hours. Finally, the TiO_2 nanobelts were obtained by post-calcination treatment for 3 h at 450 °C.

CuO/TiO_2 nanobelts. The CuO nanoparticles were incorporated on TiO_2 nanobelts using a facile wetness impregnation method. A certain amount of $Cu(NO_3)_2$ aqueous solution (10 mg mL^{-1}) was added to 0.4 g of $H_2Ti_3O_7$ nanobelts, and then ultrasonically treated for 30 min. Subsequently, the mixed solution was dried

in an oven at 110 °C for 12 hours. After that, the mixed composites with different Cu content were further calcined for 3 h at 450 °C, and the CuO/TiO_2 nanobelts were obtained. The mass contents of CuO in the CuO/TiO_2 composite materials were adjusted to be 0.1%, 0.25%, 0.5%, 1%, and 3%, which were labeled as CT-0.1, CT-0.25, CT-0.5, CT-1 and CT-3, respectively.

2.2 Characterization of samples

XRD plots were measured on a Bruker D8 Advance X-ray diffractometer with Cu Kα radiation (λ = 1.5406 Å). UV-vis DRS spectra were recorded on a Varian Cary 500 Scan UV-vis-NIR spectrometer with $BaSO_4$ as the reference. The Hitachi New Generation SU8010 field emission scanning electron microscope was used to obtain SEM images. The Brunauer–Emmett–Teller (BET) specific surface areas were determined by N_2 adsorption at 77 K on a Micromeritics ASAP 2020. XPS spectra were recorded on a VGESCALAB 250 XPS system with a monochromatized Al Kα X-ray source (15 kV 200 W 500 μm pass energy = 20 eV). All binding energies were referenced to the C 1s peak at 284.6 eV of surface adventitious carbon. HRTEM images were obtained on the JEM 2100F instrument at an accelerating voltage of 200 kV. Photo-current was measured using the conventional three-electrode electrochemical cell with a working electrode, a platinum foil counter electrode and an Ag/AgCl electrode as the reference electrode. The working electrode was fabricated on the FTO glass: 10 mg of the sample was mixed with 0.5 mL ethanol under continuous stirring for 3 h to obtain the slurry. Then, 40 μL of the slurry was spread onto FTO glass the sides of which had previously been protected by Scotch tape, and the electrode was dried at room temperature for 24 h. In the experiment, the three electrodes were immersed in a sodium sulfate electrolyte solution (0.5 M) and the working electrode was irradiated with full-spectrum light. Light/dark short circuit photocurrent response and electrochemical impedance spectroscopy (EIS) experiments were performed using an electrochemical workstation (CHI 660E).

2.3 Photocatalytic activity measurement

The photocatalytic performance of the as-prepared samples was evaluated by the degradation of MO in aqueous solution. A 300 W PLS-SXE300 Xe lamp with full-spectrum light (300–2500 nm) was used as the light source. Typically, 80 mg of the photocatalyst was added to 80 mL of 10 mg L^{-1} MO aqueous solution in a container. Prior to irradiation, the suspensions were magnetically stirred in the dark for 60 min to ensure the establishment of an adsorption/desorption equilibrium between the photo-catalyst and MO. At given irradiation time intervals, 4 mL of suspension was collected and centrifuged to remove the photo-catalyst particles, and then the residual MO solution was analyzed by monitoring variations at the wavelength of maximal absorption in the UV-vis spectra.

2.4 Active species trapping experiments

In order to probe the active species generated in the photo-catalytic reaction process, isopropanol (IPA), $Na_2C_2O_4$ and *p*-benzoquinone (BQ) as the scavengers of hydroxyl radicals ($\bullet OH$), holes (h^+) and superoxide radicals ($\bullet O_2^-$) were, respectively,

added to the MO solution to study the influence of different active species. The concentrations of IPA, $Na_2C_2O_4$ and BQ were 1 mmol L^{-1}, 1 mmol L^{-1} and 1 mmol L^{-1}, respectively. The photocatalytic degradation reaction was similar to the above test condition except for adding scavengers in the MO solution.

3 Results and discussion

The as-prepared samples were investigated by scanning electron microscopy (SEM) so as to characterize their morphologies before and after CuO surface-modification of TiO_2 nanobelts. Fig. 1 shows the SEM images of the TiO_2, CT-0.1, CT-1 and CT-3 samples. For the pure TiO_2 samples, the nanobelts are 30–60 nm in thickness, 100–300 nm in width, and the lengths range up to a few micrometers. The CT-0.1, CT-1 and CT-3 samples also display similar morphologies, which can be attributed to the low CuO loading amount. In order to verify the existence and particle size distribution of CuO, the CT-3 sample was further characterized by transmission electron microscopy (TEM). Fig. 2(a) and (b) show the TEM images of the CT-3 sample. It can be seen that the surface of TiO_2 contains some small particles, and they are
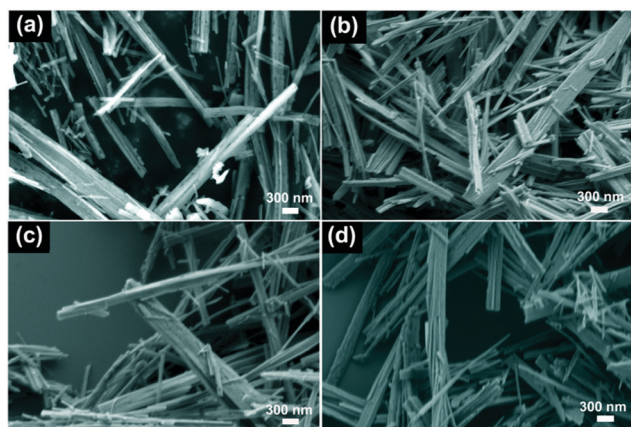

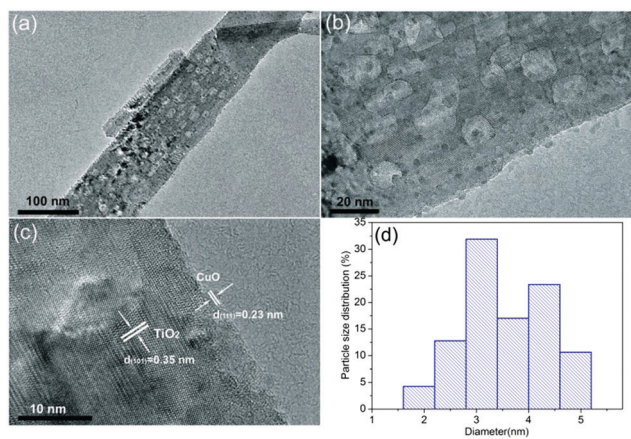Fig. 1 SEM images of (a) TiO_2, (b) CT-0.1, (c) CT-1 and (d) CT-3 samples.

Fig. 2 (a and b) TEM images of the CT-3 sample. (c) HRTEM image of the CT-3 sample. (d) Particle size distribution of CuO on the surface of TiO_2 nanobelts.
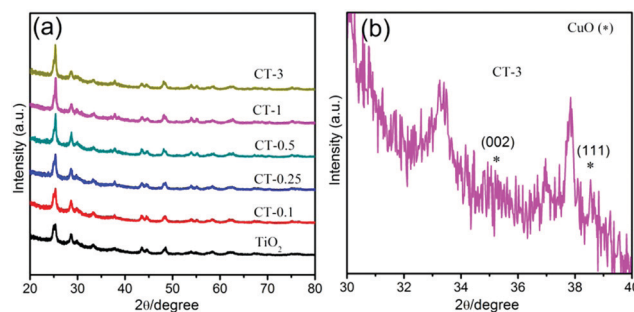
uniformly dispersed on the surface. These particles are CuO nanoparticles, which can be verified from Fig. 2(c). The distinct lattice fringes with a distance of about 0.35 nm can be observed, which is assigned to the (101) crystal plane of anatase TiO_2.[4] In addition, the lattice fringes of d-spacings of about 0.23 nm can be obtained, which is consistent with the (111) crystal plane of CuO.[24] Fig. 2(d) shows the particle size distribution of CuO on the TiO_2 nanobelts. It clearly shows that most of the CuO particles are less than 10 nanometers. These results suggest that CuO particles can be uniformly loaded on the surface of TiO_2 nanobelts via this facile strategy.

In addition, all of the as-prepared samples were further characterized by X-ray diffraction measurements (XRD), as presented in Fig. 3. Obviously, the nude TiO_2 nanobelts display the characteristic diffraction peaks of TiO_2.[34] Similarly, the CuO/TiO_2 nanobelts with different CuO contents also exhibit the characteristic diffraction peaks of TiO_2. However, new diffraction peaks appear at 35.5° and 38.7°, which are assigned to the (002) and (111) crystal planes of cubic CuO (JCPDS 45-0937),[35] as shown in Fig. 2(b). The above results suggest that the CuO/TiO_2 nanobelts with different CuO contents are successfully prepared. To investigate the influence of the specific surface area after the introduction of CuO, TiO_2 and CT-0.1 samples are further characterized by N_2 adsorption–desorption measurements, as shown in Table S1 (ESI†). Obviously, the measured specific surface areas are 54.4 and 59.3 $m^2 g^{-1}$ for TiO_2 and CT-0.1 sample, respectively. It can be concluded that the introduction of CuO doesn't obviously enhance the specific surface area of TiO_2.

XPS spectroscopy was carried out to investigate the chemical status of Ti, O and Cu elements in CuO/TiO_2 nanobelts, as displayed in Fig. 4. Fig. 4(a) presents the XPS survey spectra of the CT-3 sample, indicating that the CT-3 sample contains Ti, O and Cu elements. The high-resolution XPS spectra of Ti 2p and O 1s are shown in Fig. 4(b) and (c), respectively. It can be concluded that the two peaks at 458.6 eV and 464.3 eV are assigned to Ti $2p_{3/2}$ and Ti $2p_{1/2}$ of Ti^{4+} in TiO_2, respectively.[4] Similarly, the binding energy of the O 1s peak at 529.9 eV can be assigned to lattice oxygen, and the other peak at 530.6 eV is identified with surface hydroxyls in CuO/TiO_2.[36] Importantly, there are two peaks located at approximately 932.5 eV and 952.1 eV, corresponding to Cu $2p_{3/2}$ and Cu $2p_{1/2}$, respectively. In addition, the two satellite peaks for Cu^{2+} can also be clearly

Fig. 3 (a) XRD patterns of TiO_2 and CuO/TiO_2 nanobelts. (b) A larger version of the CT-3 sample.
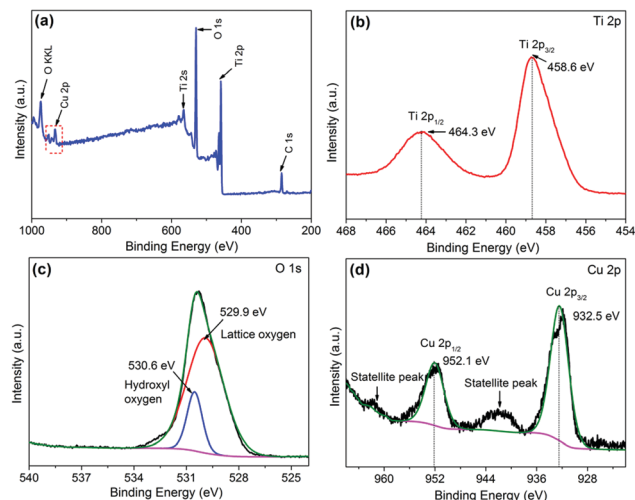
Fig. 4 (a) Typical XPS survey spectra of the CT-3 sample. The high resolution XPS spectra of Ti 2p, O 1s and Cu 2p (b, c and d, respectively) for the CT-3 sample.

observed in Fig. 4(d).[37,38] These results further confirm the existence of CuO in the CT-3 sample.

The optical absorption properties of TiO_2 and CuO/TiO_2 nanobelts were characterized in detail using ultraviolet-visible diffuse reflectance absorption spectra (DRS), as shown in Fig. 5. It can be clearly observed that the absorption band of TiO_2 nanosheets is below 400 nm assigned to the intrinsic bandgap absorption of TiO_2.[5] As expected, the photo-absorption efficiency of CuO/TiO_2 nanobelts is slightly enhanced in the visible light region after coupling with CuO nanoparticles, which is attributed to the narrower bandgap of CuO (*ca.* 1.7 eV).[39] Obviously, the visible light absorption shows a considerable improvement with the increasing CuO content in CuO/TiO_2 nanobelts. The enhanced optical adsorption of CuO/TiO_2 nanobelts is mainly ascribed to the d–d transition of Cu^{2+}.[40] It can be concluded that the special phenomenon is another piece of solid evidence to verify the existence of CuO species in the CuO/TiO_2 nanobelts.
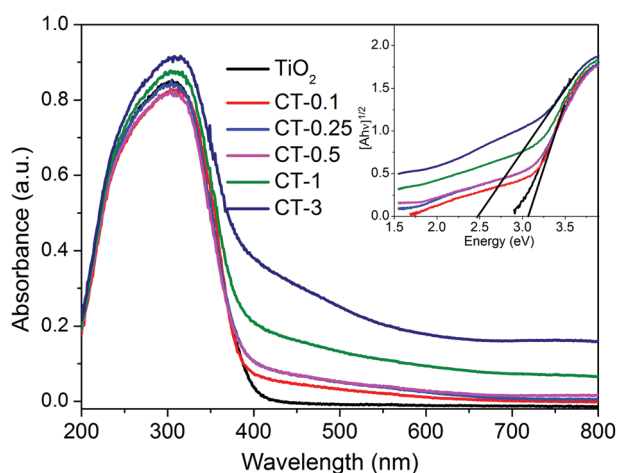

Fig. 5 UV-vis DRS spectra of TiO_2 and CuO/TiO_2 nanobelts. The inset shows the plots of $[F(R)h\nu]^{1/2}$ *versus* photon energy ($h\nu$).
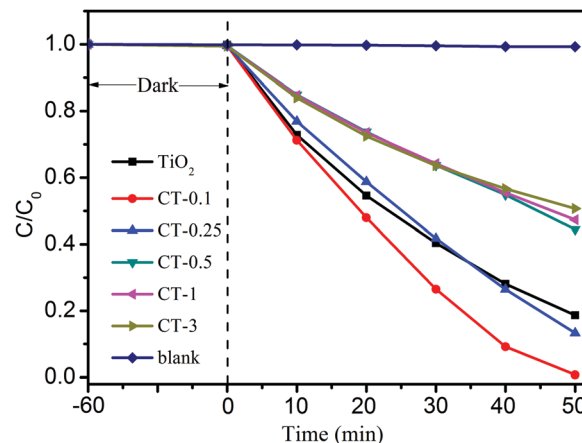

Fig. 6 Photocatalytic activity of MO degradation for TiO_2 and CuO/TiO_2 nanobelts under full-spectrum light irradiation.

The photocatalytic performance of TiO_2 and CuO/TiO_2 samples for the degradation of MO was investigated under full-spectrum light irradiation, as shown in Fig. 6. Obviously, the blank experiment shows a negligible photocatalytic activity, indicating that only MO solution can't be degraded without a photocatalyst under full-spectrum light irradiation. After coupling with CuO nanoparticles, the CuO/TiO_2 nanobelts exhibit an evident improvement with the increase of CuO content. The CT-0.1 sample displays the best photocatalytic performance compared with that of TiO_2 and the other CuO/TiO_2 nanobelts, and its degradation percent of MO reaches up to 99.2% in 50 min. Generally, the kinetics of the degradation reaction is investigated by applying the Langmuir–Hinshelwood (L–H) model.[41] The apparent reaction rate constants (k) are displayed in Table S1 (ESI†). Therein, the reaction rate constants for different samples were presented in the following order: CT-0.1 > CT-0.25 > TiO_2 > CT-0.5 > CT-1 > CT-3. It can be concluded that introducing a certain amount of CuO nanoparticles is beneficial for the photocatalytic oxidation process. However, the photocatalytic activity of CuO/TiO_2 nanobelts shows a significant decrease, when the CuO content is more than 0.25%. The reduced photocatalytic activity may be attributed to the excessive amount of CuO nanoparticles that will act as recombination centers for photo-generated electron–hole pairs. Furthermore, the stability of CT-0.1 sample was fully investigated through a cycling experiment under full-spectrum light irradiation, as indicated in Fig. S1 (ESI†). After four recycling runs, the CT-0.1 sample can still retain degradation activity, and no apparent loss can be found. This clearly indicates that the CuO/TiO_2 nanobelts have excellent stability.

In order to explore the possible reaction mechanism, the active species trapping experiments for the CT-0.1 sample were further investigated by adding some scavengers during the photocatalytic reaction process, as shown in Fig. 7. It can be easily seen that no obvious inhibiting action can be found using 1 mmol L^{-1} $Na_2C_2O_4$ as the scavenger to quench the h^+,[42] whereas the photocatalytic performance of the CT-0.1 sample has been weakening to some extent. Therein, it can be obtained that h^+ is not the major active species in the system, but it can
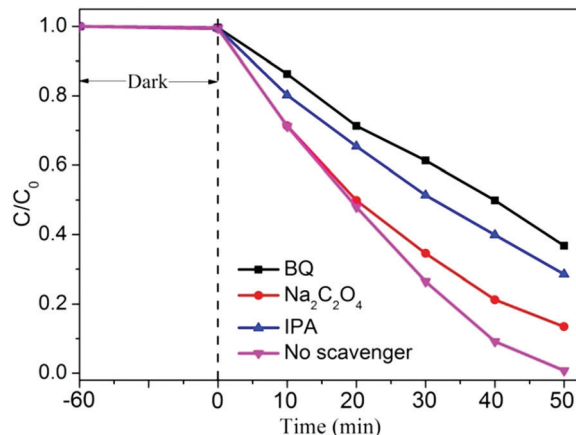
Fig. 7 Active species trapping experiment of the CT-0.1 sample in the photocatalytic reaction process.

Fig. 9 Electrochemical impedance spectroscopy (EIS) was performed using TiO$_2$ and CuO/TiO$_2$ nanobelts under full-spectrum light irradiation.

influence the photocatalytic activity of the CT-0.1 sample. Interestingly, when isopropanol (IPA) or *p*-benzoquinone (BQ) was added to the MO solution during the photocatalytic reaction process,[43] the photocatalytic activity of the CT-0.1 sample was evidently inhibited. This suggests that both superoxide radicals ($^{\bullet}O_2^{-}$) and hydroxyl radicals ($^{\bullet}OH$) are main active species, and play a decisive role during the photocatalytic degradation of MO.

The photoelectrochemical (PEC) measurement was investigated to fully elucidate the role of the CuO cocatalyst under full-spectrum light irradiation. The photocurrent response can directly reflect the generation, separation and transfer of photo-generated electron–hole pairs, which is an effective approach to monitor the interface reaction of the photocatalyst.[43,44] Fig. 8 shows the periodic on/off transient photocurrent response of TiO$_2$ and CuO/TiO$_2$ samples. Evidently, the CT-0.1 sample displays a higher photocurrent density than that of the nude TiO$_2$ and the other CuO/TiO$_2$ nanobelts, suggesting that the CT-0.1 sample possesses a much higher separation and transfer efficiency and longer lifetime of the photo-generated charge carriers. The photocurrent density follows the order of CT-0.1 > CT-0.25 > TiO$_2$ > CT-0.5 > CT-1 > CT-3.
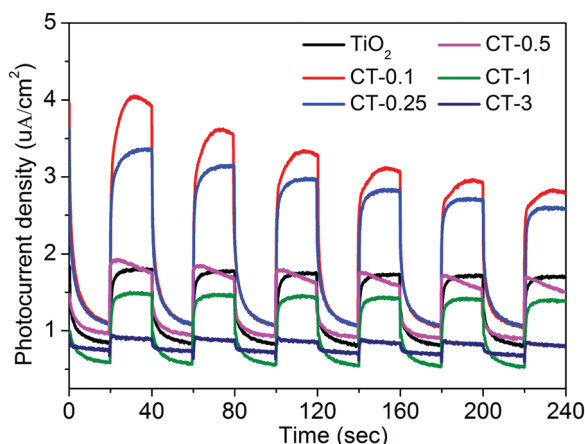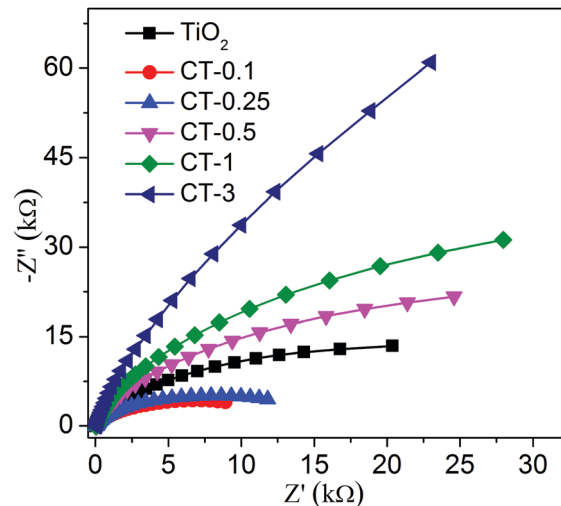

Fig. 8 Transient photocurrent responses of TiO$_2$ and CuO/TiO$_2$ nanobelts at 0 V *vs.* Ag/AgCl under full-spectrum light irradiation.

In order to further illustrate the corresponding charge transfer mechanism, electrochemical impedance spectroscopy (EIS) was carried out, as presented in Fig. 9. It is a powerful method to obtain more detailed information about the charge transport, in which the arc radius can reflect the resistance for charge transfer at the electrode/electrolyte interface.[45] Apparently, the CT-0.1 sample shows a smaller arc radius than that of TiO$_2$ and the other CuO/TiO$_2$ nanobelts, suggesting enhanced charge carrier separation and increased charge carrier mobility in line with the photocurrent measurements. Herein, the results of the photoelectrochemical measurements demonstrate that a small amount of CuO has an outstanding ability to enhance the separation and transfer of photo-generated electron–hole pairs for the composite interface. In addition, the applied potential bias-dependent photocurrent density of the TiO$_2$, CT-0.1 and CT-3 samples was implemented under full-spectrum light irradiation or dark conditions, as shown in Fig. S2 (ESI†). It can be concluded that the CT-0.1 sample displays a smaller overpotential for the oxygen production reaction in comparison with the TiO$_2$ and CT-3 samples, indicating that the lower overpotential of CT-0.1 sample may be more beneficial for the photocatalytic oxidation process. As mentioned above, it can be concluded that the CT-0.1 sample having excellent photocatalytic performance is mainly ascribed to the efficient separation and transfer of photogenerated electron–hole pairs, and low overpotential for the photocatalytic oxidation process.

In consideration of the above results, the possible photo-catalytic reaction mechanism is presented in Fig. 10. Because the work function of TiO$_2$ (4.7 eV) is smaller than that of CuO (5.3 eV),[40] a built-in electric field will be formed between TiO$_2$ and CuO, and the electric fields point out from CuO to TiO$_2$ before light irradiation.[46] When the TiO$_2$ nanobelts were irradiated by full-spectrum light, the electrons in the conduction band of TiO$_2$ will be transferred to the conduction band of CuO due to the existence of the built-in electric field. Therein, the electrons in the conduction band of CuO will reduce O$_2$ to superoxide radicals ($^{\bullet}O_2^{-}$), and the holes in the valence band of TiO$_2$ will oxidize H$_2$O

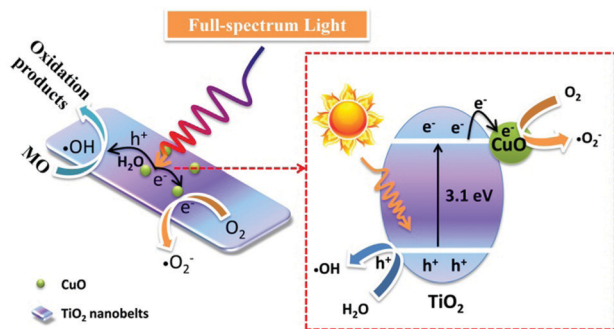**Fig. 10** Proposed mechanism for the enhanced photocatalytic activity for CuO/TiO$_2$ nanobelts.

into hydroxyl radicals (•OH) to participate in the photocatalytic degradation of MO.

4 Conclusions

In this work, CuO/TiO$_2$ nanobelts were designed and fabricated to study the photocatalytic oxidation process *via* a facile strategy. Therein, the CT-0.1 sample displays the best photocatalytic performance for the degradation of MO compared to that of nude TiO$_2$ and the other CuO/TiO$_2$ nanobelts. The enhanced photocatalytic activity is mainly attributed to the introduction of proper CuO nanoparticles. It can obviously enhance the optical absorption efficiency of TiO$_2$ nanobelts. According to the active species trapping experiments, it can be concluded that superoxide radicals (•O$_2^-$) and hydroxyl radicals (•OH) are the main active species in this photocatalytic system. In addition, the photoelectrochemical measurement demonstrates that the efficient separation and transfer of photo-generated electron–hole pairs and low over-potential of the CuO/TiO$_2$ nanobelts are beneficial for the photocatalytic oxidation process.

Conflicts of interest

There are no conflicts to declare.

Acknowledgements

Notes and references

1 L. Wang, Z. Xiao, Y. Liu, S. Cao, Z. Ma and L. Piao, *Sci. China Mater.*, 2020, **63**, 758–768.
2 H. Zhuang, W. Xu, L. Lin, M. Huang, M. Xu, S. Chen and Z. Cai, *J. Mater. Sci. Technol.*, 2019, **35**, 2312–2318.
3 Y. Wang, R. Shi, J. Lin and Y. Zhu, *Energy Environ. Sci.*, 2011, **4**, 2922–2929.
4 H. Zhuang, W. Chen, W. Xu and X. Liu, *Int. J. Energy Res.*, 2020, **44**, 3224–3230.
5 H. Zhuang, Y. Zhang, Z. Chu, J. Long, X. An, H. Zhang, H. Lin, Z. Zhang and X. Wang, *Phys. Chem. Chem. Phys.*, 2016, **18**, 9636–9644.
6 S. Wu, H. Hu, Y. Lin, J. Zhang and Y. H. Hu, *Chem. Eng. J.*, 2020, **382**, 122842.
7 C. Xu, F. Yang, B. Deng, Y. Zhuang, D. Li, B. Liu, W. Yang and Y. Li, *J. Catal.*, 2020, **383**, 1–12.
8 K. Maver, I. Arčon, M. Fanetti, S. Emin, M. Valant and U. L. Štangar, *Catal. Today*, 2020, DOI: 10.1016/j.cattod.2020.01.045.
9 J. Xue, F. Song, X. Dong, X.-W. Yin, Y. Liu, J.-M. Wu, C. Wang, X.-L. Wang and Y.-Z. Wang, *ACS Sustainable Chem. Eng.*, 2019, **7**, 1973–1979.
10 F. Yang, M. Liu, X. Chen, Z. Xu and H. Zhao, *Sol. RRL*, 2018, **2**, 1800215.
11 J. Yang, D. Wang, H. Han and C. Li, *Acc. Chem. Res.*, 2013, **46**, 1900–1909.
12 P. Zhang, T. Wang, X. Chang and J. Gong, *Acc. Chem. Res.*, 2016, **49**, 911–921.
13 Z.-K. Tang, W.-J. Yin, Z. Le, B. Wen, D.-Y. Zhang, L.-M. Liu and W.-M. Lau, *Sci. Rep.*, 2016, **6**, 32764.
14 J. Hu, P. Zhang, W. An, L. Liu, Y. Liang and W. Cui, *Appl. Catal., B*, 2019, **245**, 130–142.
15 F. M. Pesci, G. Wang, D. R. Klug, Y. Li and A. J. Cowan, *J. Phys. Chem. C*, 2013, **117**, 25837–25844.
16 S. Li, Z. Zhao, Y. Huang, J. Di, Y. Jia and H. Zheng, *J. Mater. Chem. A*, 2015, **3**, 5467–5473.
17 M. Wang, J. Han, Y. Hu and R. Guo, *RSC Adv.*, 2017, **7**, 15513–15520.
18 L. Hammarström, *Acc. Chem. Res.*, 2015, **48**, 840–850.
19 J. F. Guayaquil-Sosa, B. Serrano-Rosales, P. J. Valadés-Pelayo and H. de Lasa, *Appl. Catal., B*, 2017, **211**, 337–348.
20 L. Guo, C. Zhong, J. Cao, Y. Hao, M. Lei, K. Bi, Q. Sun and Z. L. Wang, *Nano Energy*, 2019, **62**, 513–520.
21 Z. Li, Y. Qu, K. Hu, M. Humayun, S. Chen and L. Jing, *Appl. Catal., B*, 2017, **203**, 355–362.
22 K. Wu, H. Zhu, Z. Liu, W. Rodríguez-Córdoba and T. Lian, *J. Am. Chem. Soc.*, 2012, **134**, 10337–10340.
23 N. L. Reddy, S. Emin, V. D. Kumari and S. Muthukonda Venkatakrishnan, *Ind. Eng. Chem. Res.*, 2018, **57**, 568–577.
24 L. Zhu, H. Li, Z. Liu, P. Xia, Y. Xie and D. Xiong, *J. Phys. Chem. C*, 2018, **122**, 9531–9539.
25 L. Yang, H. Li, Y. Yu and H. Yu, *Catal. Commun.*, 2018, **110**, 51–54.
26 C.-C. Hu and H. Teng, *J. Catal.*, 2010, **272**, 1–8.
27 P. Zhang, T. Wang, X. Chang, L. Zhang and J. Gong, *Angew. Chem., Int. Ed.*, 2016, **55**, 5851–5855.
28 H. Shen, D. Ni, P. Niu, Y. Zhou, T. Zhai and Y. Ma, *Int. J. Hydrogen Energy*, 2017, **42**, 30559–30568.
29 B. Çinar, I. Kerimoğlu, B. Tönbül, A. Demirbüken, S. Dursun, I. Cihan Kaya, V. Kalem and H. Akyildiz, *Mater. Sci. Semicond. Process.*, 2020, **109**, 104919.

30 Y. Li and K. Luo, *RSC Adv.*, 2019, **9**, 8350–8354.

31 K. Yao, S. Liu, Y.-Y. Dong, B. Wang, J. Bian and M.-G. Ma, *Mater. Des.*, 2016, **90**, 129–136.

32 Y. Wang, M. Zhou, Y. He, Z. Zhou and Z. Sun, *J. Alloys Compd.*, 2020, **813**, 152184.

33 Z. H. Shah, J. Wang, Y. Ge, C. Wang, W. Mao, S. Zhang and R. Lu, *J. Mater. Chem. A*, 2015, **3**, 3568–3575.

34 G. Yang, H. Ding, J. Feng, Q. Hao, S. Sun, W. Ao and D. Chen, *Sci. Rep.*, 2017, **7**, 14594.

35 X. Zhang, L. Wang, C. Liu, Y. Ding, S. Zhang, Y. Zeng, Y. Liu and S. Luo, *J. Hazard. Mater.*, 2016, **313**, 244–252.

36 J. Yuan, J.-J. Zhang, M.-P. Yang, W.-J. Meng, H. Wang and J.-X. Lu, *Catalysts*, 2018, **8**, 171.

37 Z. Liu and C. Zhou, *Prog. Nat. Sci.: Mater. Int.*, 2015, **25**, 334–341.

38 A. A. Dubale, A. G. Tamirat, H.-M. Chen, T. A. Berhe, C.-J. Pan, W.-N. Su and B.-J. Hwang, *J. Mater. Chem. A*, 2016, **4**, 2205–2216.

39 J. Liu, C. Han, X. Yang, G. Gao, Q. Shi, M. Tong, X. Liang and C. Li, *J. Catal.*, 2016, **333**, 162–170.

40 Q. Shi, G. Ping, X. Wang, H. Xu, J. Li, J. Cui, H. Abroshan, H. Ding and G. Li, *J. Mater. Chem. A*, 2019, **7**, 2253–2260.

41 X.-J. Wen, C.-G. Niu, L. Zhang and G.-M. Zeng, *ACS Sustainable Chem. Eng.*, 2017, **5**, 5134–5147.

42 W. Wang, Y. Yu, T. An, G. Li, H. Y. Yip, J. C. Yu and P. K. Wong, *Environ. Sci. Technol.*, 2012, **46**, 4599–4606.

43 H. Zhuang, Z. Cai, W. Xu, M. Huang and X. Liu, *New J. Chem.*, 2019, **43**, 17416–17422.

44 H. Zhuang, Z. Cai, W. Xu, X. Zhang, M. Huang and X. Wang, *Catal. Commun.*, 2019, **120**, 51–54.

45 J. Lin, J. Hu, C. Qiu, H. Huang, L. Chen, Y. Xie, Z. Zhang, H. Lin and X. Wang, *Catal. Sci. Technol.*, 2019, **9**, 336–346.

46 X. An, Y. Wang, J. Lin, J. Shen, Z. Zhang and X. Wang, *Sci. Bull.*, 2017, **62**, 599–601.